Faraday Discussions

Preferential destruction of NH$_2$-bearing complex interstellar molecules via gas-phase proton-transfer reactions

Journal:	*Faraday Discussions*
Manuscript ID	FD-ART-01-2023-000014.R1
Article Type:	Paper
Date Submitted by the Author:	17-Feb-2023
Complete List of Authors:	Garrod, Robin; University of Virginia, Depts. of Chemistry & Astronomy Herbst, Eric; University of Virginia, Chemistry

Journal Name

ARTICLE TYPE

Preferential destruction of NH$_2$-bearing complex interstellar molecules via gas-phase proton-transfer reactions

Robin T. Garrod*[a] & Eric Herbst[a]

Complex, nitrogen-bearing interstellar molecules, especially amines, are targets of particular interest for detection in star- and planet-forming regions, due to their possible relevance to prebiotic chemistry. However, these NH$_2$-bearing molecules are not universally detected in sources where other, oxygen-bearing complex organic molecules (COMs) are often plentiful. Nevertheless, recent astrochemical models have often predicted large abundances for NH$_2$-bearing complex organics, based on their putative production on dust grains. Here we investigate a range of new gas-phase proton-transfer reactions and their influence on the destruction of COMs. As in past studies, reactions between protonated COMs and ammonia (NH$_3$) are found to be important in prolonging gas-phase COM lifetimes. However, for molecules with proton affinities (PA) greater than that of ammonia, proton transfer reactions result in drastic reductions in abundances and lifetimes. Ammonia acts as a sink for proton transfer from low-PA COMs, while passing on protons to high-PA species; dissociative recombination with electrons then destroys the resulting ions. Species strongly affected include methylamine (CH$_3$NH$_2$), urea (NH$_2$C(O)NH$_2$) and others bearing the NH$_2$ group. The abundances of these species show a sharp time dependence, indicating that their detectability may rest on the precise chemical age of the source. Rapid gas-phase destruction of glycine (NH$_2$CH$_2$COOH) in the models suggests that its future detection may be yet more challenging than previously hoped.

1 Introduction

The presence of so-called complex organic molecules (COMs) in the interstellar medium (ISM) has been a topic of great interest and sustained discussion among astrochemists over the past several decades. COMs are typically defined as organic species composed of six or more atoms,[1] which conveniently includes methanol (CH$_3$OH), one of the most pervasive molecules observed in dense regions of the ISM. COMs are now routinely observed toward both high-mass and low-mass star-forming regions, typically through the detection of their gas-phase microwave rotational spectra. Molecules identified include methyl formate[2] (HCOOCH$_3$), dimethyl ether[3] (CH$_3$OCH$_3$), several alcohols up to and including propanol,[4,5] as well as various nitrogen-bearing species such as methylamine (CH$_3$NH$_2$)[6–8] and recently urea (NH$_2$C(O)NH$_2$).[9]

The identification of new interstellar COMs has accelerated over the past few years, due partly to the availability of the ALMA interferometer and the superlative spatial resolution and spectral sensitivity that it offers. Meanwhile, many very recent COM detections have been driven by a dedicated, deep-integration line survey of the Galactic Center cloud G+0.693-0.027 using single-dish instruments. While G+0.693 is quiescent (i.e. non-star forming), the plethora of COMs found toward this object are thought to result from the disruption of molecule-rich dust-grain ice mantles, caused by the passage of low-velocity shocks;[10,11] thermal desorption and/or sputtering of these molecules from the grains would allow them to be detected by rotational spectroscopy as well as making them available for possible gas-phase chemistry. Recent new detections toward this source include a selection of nitrogen-bearing molecules such as hydroxylamine[12] (NH$_2$OH), vinylamine (C$_2$H$_3$NH$_2$) and ethylamine[13] (C$_2$H$_5$NH$_2$), and ethanolamine[14] (NH$_2$CH$_2$CH$_2$OH).

These latter species, along with several others, retain particular interest due to the importance of the amine (–NH$_2$) group in biochemical compounds, and thus the possibility that certain important pre-biotic molecules may have had an interstellar origin. Perhaps chief among such targets for interstellar detection over the past decades – partly due to its totemic value – has been glycine (NH$_2$CH$_2$COOH), the simplest amino acid. Unfortunately, in spite of various searches,[15–18] interstellar glycine remains elusive, although it has now been detected in two comets within our own solar system.[19,20] Chemical kinetic simulations of star-forming regions have nevertheless predicted the presence of modest amounts of glycine on interstellar dust grains,[21–23] with the expectation that the heating caused by the star-formation process might allow it to be released, and thus detected in the gas

[a] Depts. of Chemistry & Astronomy, University of Virginia, Charlottesville, VA 22904, USA; E-mail: rgarrod@virginia.edu

phase given sufficient observing power. While other NH_2-bearing species are now beginning to be detected, in particular toward G+0.693, even simpler species like methylamine are by no means ubiquitous in the usual hot core sources, while hydroxylamine has not yet been detected toward a star-forming source.[24]

COMs are most typically detected toward hot, star-forming cores, known as hot cores and hot corinos, in the case of high-mass and low-mass sources, respectively. The rich molecular emission spectra of these sources indicate various COMs reaching abundances as high as 10^{-7} with respect to total hydrogen, with excitation temperatures upward of 100 K (hence "hot"). While there continues to be much debate over the origins of specific molecules,[25] the general picture of the chemistry of hot cores involves firstly the formation of ice mantles on the surfaces of dust grains, fed by surface chemistry involving atoms and molecules adsorbed from the gas phase at temperatures of the order of 10 K. This is followed by a period of warming, driven by the evolution of the nascent protostar, that allows the thermal release of the molecules from the grain surfaces and thence their spectroscopic detection at temperatures reflective of the ambient hot conditions. This release also promotes further gas-phase chemistry. However, while undoubtedly many observed molecules are formed strongly in the gas-phase during this hot period (including some COMs, e.g. dimethyl ether[26]), much research now points to a substantially earlier, cold grain-surface chemistry as the origin of perhaps the greater part of the inventory of detected COMs, particularly O-bearing species.[26–31]

Regardless of the originating formation mechanisms, gas-phase COMs are subject to destructive processes involving ion-driven chemistry. The dominant destruction pathways for COMs begin with proton transfer (PT) reactions with abundant ions such as H_3^+, H_3O^+, and HCO^+; the latter two are formed strongly when abundant ice species H_2O and CO are released into the gas, undergoing proton transfer from H_3^+ (whose own origins lie in the cosmic ray ionization of gas-phase molecular hydrogen). Due to the large abundance of water in particular ($\sim 10^{-4} n_H$), following its desorption from the grains, the dominant PT reactions undergone by COMs tend to involve H_3O^+, which is the most abundant cation in the gas at that point. The protonated COMs may then undergo dissociative recombination (DR) with electrons, which typically breaks down the structure of the underlying molecule; only a small fraction of recombinations lead to the simple ejection of an H atom and the reformation of the COM,[27,32] with three or more fragments being typical. Thus, the gas-phase abundances of COMs would be expected to degrade gradually over time, especially if no efficient mechanism of gas-phase production is available following their desorption from the grains.

Proton transfer reactions, when exothermic, typically occur at around the collisional rate,[35] which is usually of the order of 10^{-9} cm^3 s^{-1} at 300 K. For a given PT reaction, $AH^+ + B \rightarrow A + BH^+$, the enthalpy change associated with the reaction can be determined from the difference in proton affinities (PA) of the reactant and product neutrals; Table 1 shows a selection of such values. Astrochemical networks have typically included all energetically favourable (exothermic) PT processes between COMs and the abundant gas-phase ions H_3^+, H_3O^+, and HCO^+.[26] The

Table 1 Proton affinites for a selection of chemical species, used in the calculation of new proton transfer rates; species marked † are included in the special set of additional reactions used in model M5, either as reactants or as products of reactions involving their protonated forms.

Molecule	Proton Affinity (kJ mol^{-1})	Reference
H_2	422.3	Hunter and Lias [33]
CO (at C atom)	594.0	Hunter and Lias [33]
H_2O	691.0	Hunter and Lias [33]
CH_3OH †	754.3	Hunter and Lias [33]
CH_3CN	779.2	Hunter and Lias [33]
$HCOOCH_3$	782.5	Hunter and Lias [33]
CH_3OCH_3	792.0	Hunter and Lias [33]
NH_2OH †	810.4	CCCBDB database‡
NH_2CHO	822.2	Hunter and Lias [33]
CH_3NC †	839.1	Hunter and Lias [33]
H_2SiO †	841.0	Hunter and Lias [33]
NH_2OCH_3 †	844.8	Hunter and Lias [33]
NH_2CH_2OH †	844.8	Estimate
C_2H_5NC †	851.3	Hunter and Lias [33]
CH_3NHCHO †	851.3	Hunter and Lias [33]
CH_2NH †	852.9	Hunter and Lias [33]
N_2H_4 †	853.2	Hunter and Lias [33]
NH_3 †	853.6	Hunter and Lias [33]
NH_2CH_2CHO †	856.0	Estimate
$NH_2C(O)CHO$ †	860.0	Estimate
$NH_2C(O)OCH_3$ †	860.0	Estimate
$NH_2C(O)CH_2OH$ †	860.0	Estimate
$CH_3C(O)NH_2$ †	863.6	Hunter and Lias [33]
$NH_2C(O)NH_2$ †	868.4	Zeng and Cooks [34]
C_2S †	869.6	Hunter and Lias [33]
C_3O †	880.2	Hunter and Lias [33]
NH_2CH_2COOH †	886.5	Hunter and Lias [33]
CH_3NH_2 †	899.0	Hunter and Lias [33]
$C_2H_5NH_2$ †	912.0	Hunter and Lias [33]
C_3S †	933.0	Hunter and Lias [33]
$NaOH$ †	1071.8	Hunter and Lias [33]

$\ddagger$ Computational Chemistry Comparison and Benchmark DataBase of the National Institute of Standards and Technology (NIST)

low PAs of H_2, H_2O and CO ensure that proton transfer is usually effective in all three cases. For example, for a proton transfer from water (PA=691.0 kJ mol^{-1}) to methanol (PA=754.3 kJ mol^{-1}),

$$H_3O^+ + CH_3OH \rightarrow CH_3OH_2^+ + H_2O \tag{1}$$

the change in enthalpy is -63.3 kJ mol^{-1}, indicating a strongly exothermic process that proceeds unimpeded at the collisional rate. In cases where the difference in proton affinity is more extreme, such as for reactions between H_3^+ and COMs, corresponding to the transfer of a proton from H_2 (PA=422.3 kJ mol^{-1}) to a COM, the exothermicity may be so great as to result in the breakup of the products, with simple proton transfer being only a minor branch, e.g.,[36]

$$H_3^+ + CH_3OH \rightarrow CH_3^+ + H_2O + H_2 \ (46\%)$$

$$\rightarrow CH_2OH^+ + 2\,H_2 \ (28\%)$$

$$\rightarrow CH_3OH_2^+ + H_2 \ (26\%)$$
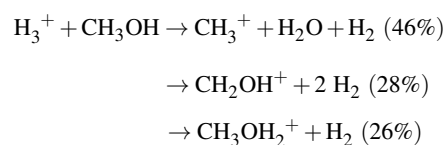
where the change in enthalpy for the third branch, provided by the difference in proton affinities, is -332 kJ mol^{-1}. For reactions of H_3O^+ and HCO^+ with COMs, the destruction of the PT products typically does not occur,[35] as the higher PA of the underlying

Table 2 Description of chemical models run, based on the chemical reaction network adopted. For each model M0, M1, etc., a single cold collapse simulation (Stage 1) is run, followed by a warm-up (Stage 2) using one of three characteristic timescales (*fast*, *medium* and *slow*).

Model	Description
M0	No proton transfer (PT) reactions involving COMs (aside from the usual H_3^+, H_3O^+ and HCO^+ reactions, as per past models).
M1	Same as the `final` model of Garrod *et al.* (2022);[23] exothermic PT reactions from protonated molecules to NH_3 are allowed.
M2	Exothermic PT reactions from protonated molecules to NH_3, and from NH_4^+ to neutral molecules, are included.
M3	As M2, with exothermic PT reactions from protonated molecules to CH_3OH, and from $CH_3OH_2^+$ to neutral molecules are included.
M4	Both exothermic and endothermic PT reactions from protonated molecules to NH_3 and CH_3OH, and from NH_4^+ and $CH_3OH_2^+$ to neutral molecules, are included.
M5	As M4, with all PT reactions included for which either the neutral reactant or product molecule has proton affinity close to or greater than $PA(NH_3)$.

H_2O or CO molecule makes the exothermicity of the reaction less extreme. Thus, due to the position of H_3O^+ as the leading ionic reaction partner for COMs, direct PT dominates over any possible alternative destruction outcomes.

For a COM such as methanol, its main gas-phase destruction pathway following desorption would therefore proceed firstly through protonation via Eq. (1), then through dissociative recombination of the resultant protonated methanol with electrons. The latter process has a number of branches, most of which irretrievably break down the original structure:[27]

$$CH_3OH_2^+ + e^- \rightarrow CH_3 + OH + H \ (51 \pm 4\%)$$
$$\rightarrow CH_2 + H_2O + H \ (21 \pm 2\%)$$
$$\rightarrow H_2CO + H_2 + H \ (10 \pm 1\%)$$
$$\rightarrow CH_3 + H_2O \ (9 \pm 2\%)$$
$$\rightarrow CH_3O + H_2 \ (6 \pm 2\%)$$
$$\rightarrow CH_3OH + H \ (3 \pm 2\%)$$
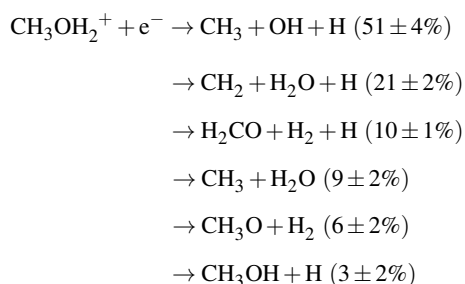
An important development in the astrochemical modelling of hot cores came with the work of Taquet *et al.*,[37] who included in their chemical network various additional PT reactions, involving a selection of COMs and abundant simple molecules, along with the protonated forms of each. This allowed for protonated COMs to react with other molecular species of higher PA, including the abundant methanol and ammonia released from the grains during the hot stage, thus introducing an alternative to electronic DR. Due to the higher PA of methanol and ammonia (versus e.g. H_2, CO or H_2O), their involvement in PT reactions with COMs, either as reactants or products, should typically involve smaller exothermicities, and thus a small likelihood of break-up rather than proton transfer; the somewhat limited experimental evidence available seems to confirm this expectation[35,38] (see also Sec. 2.3).

In their astrochemical models, Taquet *et al.* found that ammonia in particular, due to its large proton affinity and substantial abundance, would act as an important acceptor of protons from many species; for example, from protonated methanol:

$$CH_3OH_2^+ + NH_3 \rightarrow NH_4^+ + CH_3OH$$
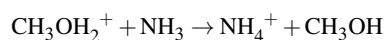
which is exothermic, with an enthalpy change of -99.3 kJ mol^{-1}.

These proton transfer reactions between ammonia and various protonated COMs would return the underlying molecule to its original state, without destruction. They are also highly competitive with electronic DR, thus diminishing the main process of de-struction for those COMs and extending their gas-phase lifetimes considerably.

In the model of Taquet *et al.*, NH_3 was the species of highest PA, meaning that the cascade of proton transfer from various protonated molecules would terminate with ammonia. In spite of the resulting increase in conversion of NH_3 to NH_4^+, dissociative recombination of the latter typically leads only to the ejection of an H atom, allowing ammonia abundances to remain relatively stable.

A selection of proton-transfer reactions between protonated COMs and ammonia was incorporated into the recent hot-core models of Garrod *et al.* (2022);[23] these authors presented an advanced treatment of grain-surface and ice chemistry in which many COMs could be formed at low temperatures on the grains, as the result of so-called nondiffusive reactions (often via radical-radical recombination). As in the work of Taquet *et al.*, they found that the inclusion of the ammonia-related PT reactions produced a strong effect on the peak gas-phase abundance attained by methyl formate, one of the key COMs observed in hot cores, as well as an increase in the gas-phase lifetimes of COMs in general, particularly the O-bearing species, which have relatively low PAs.

The models of Garrod *et al.*[21,23,26] are fairly unique in simulating the gas and grain-surface chemistry of a large selection of COMs, including NH_2-bearing species such as methylamine, ethylamine, acetamide ($CH_3C(O)NH_2$), urea, and even glycine. However, as may be seen from Table 1, these species have substantially larger PAs than ammonia. This means firstly that proton transfer to ammonia from their protonated forms is not energetically favourable; thus, such processes were not considered in the above networks, and the underlying COMs did not experience enhanced abundances as a result. Secondly, it means that a full reckoning of their chemistry must make allowance for proton transfer from NH_4^+ to those COMs, thus *increasing* their rates of destruction via protonation and dissociative recombination. PT reactions of those COMs with other protonated species, including those of other COMs (of lower PA), should also have a similar effect. In principle, the inclusion of PT reactions involving other species with even greater PA could also influence the behaviour of all the others, dependent on their abundances.

Some important gas-phase reaction mechanisms therefore appear to be missing from the existing networks, which may have a strong influence on the expected gas-phase abundances of NH_2-bearing species in particular. This effect would also be of interest due to the overproduction of certain nitrogen-bearing species in the models; these include hydroxylamine[21,24] and urea.[9] Given

the large PA of glycine, the possibility of its future interstellar detection may also depend on the outcome of gas-phase proton-transfer reactions.

In the present study, we introduce new proton transfer reactions incrementally into the network of Garrod *et al.* (2022).[23] The networks are implemented in the three-phase gas-grain astrochemical model *MAGICKAL*, with model runs applied to generic, hot-core physical treatments. Analysis of the results focuses especially on nitrogen-bearing species.

2 Methods

2.1 Chemical model

Chemical kinetic simulations of coupled gas-phase, grain-surface and bulk-ice (i.e. three-phase) chemistry in hot, star-forming cores are carried out using the *MAGICKAL* code;[21] the latter has undergone significant updates since its inception, described in detail by Garrod *et al.* (2022,[23] hereafter G22). The most significant changes involve the introduction of nondiffusive reaction mechanisms on grain surfaces and in the ice mantles that build up on the grains during the early, cold stages of the models. Past hot core models involving grain-surface chemistry have been based largely on diffusive chemistry, in which grain-surface chemical reactions are dominated by H diffusion at the lowest temperatures, leading to the production of hydrides such as water, methane and ammonia. At elevated temperatures (>20 K), the production of COMs in those models depended on surface diffusion of reactive radicals including CH_3, HCO and NH_2 to build up molecular structures group by group. While the present models still retain these diffusion-driven reaction processes, they no longer require grain-surface reactions to occur solely as the result of diffusive meetings; instead, a reactive species may be *formed* in a position close or contiguous to a potential reaction partner, leading to an instantaneous follow-on reaction without the need for diffusion across the surface. The driving rates for nondiffusive reactions are therefore determined either by the rate of some initiating reaction, or by the rate of photodissociation of some precursor species, either of which may result in the formation of a chemical species that in some fraction of cases happens to be formed next to its subsequent reaction partner. The formulation for the inclusion of these mechanisms in the models is described in detail by Jin & Garrod (2020).[31]

Within the framework of the physical conditions used to represent the hot core environment (see Sec. 2.2), six sets of chemical models are run, each using a different chemical network setup (see Table 2 and Sec. 2.3). The number of chemical species in all the model runs remains the same: a total of 1385, which comprises 749 gas-phase species, along with 318 neutrals in the dust-grain surface layer and the same number in the bulk ice component. The surface layer is restricted to a maximum of 1 monolayer thickness; net growth in the surface component leads to the transfer of material into the bulk beneath, while a net loss results in transfer from the bulk back into the surface layer,[39] such as during the warm-up stage when the ice mantles desorb into the gas phase. The chemical network used in the basic (M1) model presented here comprises a total of 22,401 reactions and pro-

Table 3 Initial, gas-phase chemical abundances with respect to total hydrogen, applied at the beginning of the collapse stage (Stage 1).

Chemical species, i	n_i/n_H
H	2×10^{-3}
H_2	0.499
He	9×10^{-2}
C	1.4×10^{-4}
N	7.5×10^{-5}
O	3.2×10^{-4}
S^+	8×10^{-8}
Si^+	8×10^{-9}
Fe^+	3×10^{-9}
Na^+	2×10^{-8}
Mg^+	7×10^{-9}
P^+	3×10^{-9}
Cl^+	4×10^{-9}

cesses, which include but are not limited to a range of gas-phase reactions, adsorption and desorption, transfer between surface and bulk ice, photodissociation of gas-phase, surface and bulk-ice molecules, and reactions on the surface and in the bulk ice. The models presented in this work use the same set of chemical initial conditions as in past models, such as G22, as listed in Table 3. The assumed gas:dust ratio by mass is 100, with a representative grain radius of 0.1 μm and 10^6 grain-surface binding sites.

The reaction rate coefficients of all gas-phase reactions used in the networks presented here use the modified Arrhenius form:

$$k = \alpha \left(\frac{T}{300 \text{ K}} \right)^{\beta} \exp \left(-\frac{\gamma}{k_b T} \right) \qquad (2)$$

2.2 Physical model

To replicate the time-dependent behaviour of the physical conditions within a hot core, a typical two-stage model is used.[40] The collapse stage, Stage 1, begins with a gas density $n_H = 3000$ cm^{-3} and visual extinction $A_V = 3$. The gas temperature is fixed at 10 K during this stage. The density and extinction evolve according to an isothermal freefall collapse, reaching final values 2×10^8 cm^{-3} and 500 mag., respectively, over a period lasting $\sim 10^6$ yr. Dust temperature is calculated as a function of the time-dependent visual extinction,[41] beginning at ~ 14.6 K and falling to 8 K. The Stage 1 simulation begins from the chemical conditions given in Table 3, with all other species nominally at zero abundance, and the electron fraction set to the sum of the cation abundances.

The final chemical abundances calculated in Stage 1 are used as the starting point for the warm-up stage, Stage 2. During Stage 2, the gas density and visual extinction are held steady at the final Stage 1 values. Meanwhile, the gas and dust temperatures rise monotonically, from the $T_{gas} = 10$ K and $T_{dust} = 8$ K values achieved at the end of Stage 1 up to $T_{gas} = T_{dust} = 400$ K (T_{dust} rises independently until $T_{dust} = T_{gas}$, then they rise together). Following past treatments, three characteristic warm-up timescales are employed, resulting in three different Stage 2 runs for each Stage 1 collapse. The timescales correspond to the time taken to reach 200 K, and are labelled *fast* (5×10^4 yr), *medium* (2×10^5 yr) and *slow* (1×10^6 yr). This warm-up is intended to reproduce the gradual warming experienced by the dust and gas as the central

Table 4 Selected proton transfer reactions added to the chemical networks, and their reaction parameters as applied to Eq. (2). The enthalpy change of the reaction, ΔH_r, is provided, based on the difference in proton affinities of the reactant and product neutrals. The final column indicates the first of the presented models in which the listed reaction first appears.

Reaction							ΔH_r (kJ mol^{-1})	α (cm^3 s^{-1})	β	γ (K)	Model
$CH_3OH_2^+$	+	NH_3	$\rightarrow$	NH_4^+	+	CH_3OH	-99.3	1.85×10^{-9}	-0.5	0	M1
$[HCOOCH_3]H^+$	+	NH_3	$\rightarrow$	NH_4^+	+	$HCOOCH_3$	-71.1	1.70×10^{-9}	-0.5	0	M1
$CH_3OCH_4^+$	+	NH_3	$\rightarrow$	NH_4^+	+	CH_3OCH_3	-61.6	1.76×10^{-9}	-0.5	0	M1
$NH_2OH_2^+$	+	NH_3	$\rightarrow$	NH_4^+	+	NH_2OH	-43.2	1.84×10^{-9}	-0.5	0	M1
NH_2CHOH^+	+	NH_3	$\rightarrow$	NH_4^+	+	NH_2CHO	-31.4	1.75×10^{-9}	-0.5	0	M1
NH_4^+	+	$CH_3C(O)NH_2$	$\rightarrow$	$CH_3C(O)NH_3^+$	+	NH_3	-10.0	3.91×10^{-9}	-0.5	0	M2
NH_4^+	+	$NH_2C(O)NH_2$	$\rightarrow$	$NH_2C(O)NH_3^+$	+	NH_3	-14.8	3.98×10^{-9}	-0.5	0	M2
NH_4^+	+	NH_2CH_2COOH	$\rightarrow$	$NH_2CH_2COOH_2^+$	+	NH_3	-32.9	1.22×10^{-9}	-0.5	0	M2
NH_4^+	+	CH_3NH_2	$\rightarrow$	$CH_3NH_3^+$	+	NH_3	-45.4	1.51×10^{-9}	-0.5	0	M2
NH_4^+	+	$C_2H_5NH_2$	$\rightarrow$	$C_2H_5NH_3^+$	+	NH_3	-58.4	1.51×10^{-9}	-0.5	0	M2
$CH_3OH_2^+$	+	$HCOOCH_3$	$\rightarrow$	$[HCOOCH_3]H^+$	+	CH_3OH	-28.2	1.48×10^{-9}	-0.5	0	M3
$CH_3OH_2^+$	+	CH_3OCH_3	$\rightarrow$	$CH_3OCH_4^+$	+	CH_3OH	-37.7	1.16×10^{-9}	-0.5	0	M3
$CH_3OH_2^+$	+	NH_2OH	$\rightarrow$	$NH_2OH_2^+$	+	CH_3OH	-56.1	5.61×10^{-10}	-0.5	0	M3
$CH_3OH_2^+$	+	NH_2CHO	$\rightarrow$	NH_2CHOH^+	+	CH_3OH	-67.9	3.30×10^{-9}	-0.5	0	M3
$CH_3OH_2^+$	+	$CH_3C(O)NH_2$	$\rightarrow$	$CH_3C(O)NH_3^+$	+	CH_3OH	-109.3	3.16×10^{-9}	-0.5	0	M3
$CH_3OH_2^+$	+	$NH_2C(O)NH_2$	$\rightarrow$	$NH_2C(O)NH_3^+$	+	CH_3OH	-114.1	3.21×10^{-9}	-0.5	0	M3
$CH_3OH_2^+$	+	NH_2CH_2COOH	$\rightarrow$	$NH_2CH_2COOH_2^+$	+	CH_3OH	-132.2	9.69×10^{-10}	-0.5	0	M3
$CH_3OH_2^+$	+	CH_3NH_2	$\rightarrow$	$CH_3NH_3^+$	+	CH_3OH	-144.7	1.28×10^{-9}	-0.5	0	M3
$CH_3OH_2^+$	+	$C_2H_5NH_2$	$\rightarrow$	$C_2H_5NH_3^+$	+	CH_3OH	-157.7	1.24×10^{-9}	-0.5	0	M3
NH_4^+	+	N_2H_4	$\rightarrow$	$N_2H_5^+$	+	NH_3	0.4	1.99×10^{-9}	-0.5	50.3	M4
NH_4^+	+	NH_2CHO	$\rightarrow$	NH_2CHOH^+	+	NH_3	31.4	4.02×10^{-9}	-0.5	3770	M4
$NH_2C(O)NH_3^+$	+	NH_3	$\rightarrow$	NH_4^+	+	$NH_2C(O)NH_2$	14.8	1.70×10^{-9}	-0.5	1810	M4
$NH_2CH_2COOH_2^+$	+	NH_3	$\rightarrow$	NH_4^+	+	NH_2CH_2COOH	32.9	1.66×10^{-9}	-0.5	3980	M4
$[HCOOCH_3]H^+$	+	CH_3OH	$\rightarrow$	$CH_3OH_2^+$	+	$HCOOCH_3$	28.2	1.43×10^{-9}	-0.5	3370	M4
CH_3CNH^+	+	CH_3OH	$\rightarrow$	$CH_3OH_2^+$	+	CH_3CN	24.9	1.54×10^{-9}	-0.5	2970	M4
$CH_3OH_2^+$	+	$NaOH$	$\rightarrow$	$NaOH_2^+$	+	CH_3OH	-317.5	5.82×10^{-9}	-0.5	0	M5
NH_4^+	+	$NaOH$	$\rightarrow$	$NaOH_2^+$	+	NH_3	-218.2	7.02×10^{-9}	-0.5	0	M5
$NH_2CH_2COOH_2^+$	+	CH_3NH_2	$\rightarrow$	$CH_3NH_3^+$	+	NH_2CH_2COOH	-12.5	1.10×10^{-9}	-0.5	0	M5
$CH_3NH_3^+$	+	NH_2CH_2COOH	$\rightarrow$	$NH_2CH_2COOH_2^+$	+	CH_3NH_2	12.5	1.00×10^{-9}	-0.5	1510	M5
$CH_3NH_3^+$	+	$C_2H_5NH_2$	$\rightarrow$	$C_2H_5NH_3^+$	+	CH_3NH_2	-13.0	1.28×10^{-9}	-0.5	0	M5
$C_2H_5NH_3^+$	+	CH_3NH_2	$\rightarrow$	$CH_3NH_3^+$	+	$C_2H_5NH_2$	13.0	1.19×10^{-9}	-0.5	1560	M5
$CH_3NH_3^+$	+	$NaOH$	$\rightarrow$	$NaOH_2^+$	+	CH_3NH_2	72.8	5.98×10^{-9}	-0.5	0	M5

protostar evolves, over a plausible range of timescales; the precise warm-up timescale for individual sources is rather uncertain. Comparison of model results with observed molecular abundance ratios by G22 indicates that longer warm-up timescales are more consistent with hot core abundances, while shorter timescales provide a better match with values observed in the lower-mass hot corinos. We refer the reader to Garrod & Herbst (2006)[40] and G22 for more detail and discussion of these points.

2.3 Implementation of new proton-transfer reactions

Using the above-described chemical and physical setups, six different chemical networks are tested, which vary only in the number of proton-transfer reactions included. The models (Stage 1 + Stage 2) using these different chemical networks are labelled M0 – M5 (see Table 2). Descriptions of these models follow below. Table 4 shows a selection of the reactions that were added to the chemical network used in each model; the reactions shown are not comprehensive, but serve to illustrate the types of reactions added. Rate coefficients are also indicated for each reaction.

Models M0 and M1: The model M1 setup is identical to the `final` model setup of G22, and is used as a reference point; the associated chemical network includes exothermic PT reactions of protonated COMs (and other protonated species) with ammonia. In order to demonstrate the influence of those reactions alone, model M0 is also presented here, corresponding to the absence of those NH_3-related reactions in an otherwise identical setup (no such model was explicitly presented by G22).

In the M1 model network, in which reactions of the form $AH^+ + NH_3 \rightarrow A + NH_4^+$ are included, species "A" is selected from a list of $\sim$300 neutral species in the network that have a known PA (or an approximate value), and that have a protonated form also included in the network; from these, only those species with a PA less than that of ammonia are included.

Model M2: Model M2 is the same as M1, except that its chemical network also includes exothermic PT reactions between NH_4^+ and neutral COMs chosen from the same basic set of $\sim$300 potential reactants. For the reactions $NH_4^+ + A \rightarrow NH_3 + AH^+$, the set of species "A" used in the network includes only COM species with PA greater than that of ammonia, of which there are nine; all such species in the network are shown in Table 1, listed beneath ammonia. There are few experimental examples of such reactions, perhaps partly due to the limited num-

ber of COMs with sufficiently high PA. However, the reaction $NH_4^+ + CH_3NH_2 \rightarrow CH_3NH_3^+ + NH_3$ has been tested several times in the laboratory,[42–45] with proton transfer occuring in 100% of cases. The measured reaction rate ranges from 1.40–2.50×10^{-9} cm^3 s^{-1} at 300 K. The calculated value used in our networks is $1.5 \times 10^{-9} (T/300\,\text{K})^{-1/2}$ cm^3 s^{-1} (see Sec. 2.3.1).

The non-COM species in the network with PA greater than PA(NH$_3$), i.e. C$_2$S, C$_3$O, C$_3$S and NaOH, do not have reactions added at this stage.

In a number of cases (relevant to all Models M1 – M5) proton affinities were not available in the literature. For each species that was expected to have a PA value close to or greater than that of ammonia, a crude estimate was made for the purposes of the present work (as indicated in Table 1), based on relative values between similar species with some of the same functional groups, e.g. PA(NH$_2$C(O)OCH$_3$) $\simeq$ PA(NH$_2$C(O)NH$_2$) $-$ (PA(N$_2$H$_4$) $-$ PA(NH$_2$OCH$_3$)). Since these estimated values happen to be close to PA(NH$_3$), they should be regarded with caution, and we do not linger on the results for those species; the associated PT reactions are included mainly for purposes of completeness.

In cases where two protonated forms of a COM exist in the network, branching is assumed to be statistical.

Model M3: Model M3 in addition includes a similar set of exothermic PT reactions involving reactions of CH$_3$OH and CH$_3$OH$_2^+$ with protonated species and neutrals, respectively. Whether the reaction included in the network corresponds to proton transfer to or from methanol is determined by the relative PAs of methanol and the other neutral. Due to the lower proton affinity of methanol with respect to ammonia, a larger set of neutrals is able to accept a proton from methanol than from ammonia. However, the resulting protonated species would in turn be able to transfer a proton exothermically to ammonia.

Model M4: Model M4 includes the same exothermic reactions involving NH$_3$, NH$_4^+$, CH$_3$OH and CH$_3$OH$_2^+$, but also introduces a selection of PT reactions that are moderately endothermic, defined here as ΔPA < 41 kJ mol^{-1} (i.e. $\sim$5000 K). Thus, in cases where only a small difference in PA exists between reactant and product neutrals, the backward reaction is also included in the network along with its exothermic counterpart. In these cases, the rate coefficient of the backward PT reaction may become comparable to that of the forward reaction given sufficient temperature.

Model M5: In Model M5, a more comprehensive network is used, which allows exothermic and endothermic PT reactions to take place between a much broader range of species, based around those listed in Table 1. For all PT reactions AH$^+$ + B $\rightarrow$ A + BH$^+$ and their reverse reactions, species "A" is drawn from the basic list of $\sim$300 viable neutrals in the network, while species "B" is drawn from the list shown in Table 1 (marked †) for which the PA is greater than or close to that of ammonia. This list includes also the four non-COM species with PA greater than PA(NH$_3$). Added to this list also is hydroxylamine (NH$_2$OH), which is included due to its particular astronomical interest (see Sec. 4). Species set "B" is a subset of set "A", thus PT reactions amongst all species marked † in Table 1 are included, either in one direction or both. Species in set "A" that are not members of set "B"

Table 5 Selected dust-grain ice abundances achieved at the end of the M1 Stage 1 model. Abundances for these species are identical among models M0 – M5. Commonly observed ice species are shown in the upper half of the table; selected species/COMs of interest are shown in the lower half. Abundances are given as a fraction of total hydrogen in the simulation, and as a percentage of water ice. Notation $a(-b)$ indicates $a \times 10^{-b}$.

Ice species, i	n_i/n_H	% / water ice
H$_2$O	1.63(-4)	100
CO	5.42(-5)	33.0
CO$_2$	3.36(-5)	20.6
CH$_4$	9.08(-6)	5.57
NH$_3$	2.81(-5)	17.2
H$_2$CO	2.98(-6)	1.83
CH$_3$OH	9.58(-6)	5.88
CH$_3$CN	8.97(-10)	5.50(-4)
NH$_2$CHO	1.15(-8)	7.24(-3)
NH$_2$OH	3.95(-6)	2.42
HCOOCH$_3$	1.12(-7)	6.87(-2)
CH$_3$OCH$_3$	8.07(-8)	4.95(-2)
CH$_3$NH$_2$	3.96(-7)	2.43(-1)
C$_2$H$_5$NH$_2$	2.46(-8)	1.15(-2)
CH$_3$C(O)NH$_2$	3.64(-9)	2.23(-3)
NH$_2$C(O)NH$_2$	7.46(-9)	4.58(-3)
NH$_2$CH$_2$COOH	2.93(-10)	1.80(-4)

therefore are not, in general, allowed to undergo proton-transfer amongst each other, except in the case of reactions with small molecular ions such as H$_3^+$, etc. The large gas-phase abundances of ammonia and methanol are assumed to render such reactions relatively unimportant.

2.3.1 Calculation of proton transfer rate coefficients

For the few PT reactions involving apolar neutral species, collisional rate coefficients are calculated as straightforward Langevin values, with polarizabilities determined from the literature. For the majority of newly added reactions, the neutrals are polar; in these cases the ADO formulation is used,[46] with the assumption that the permanent-dipole term vastly outweighs the Langevin term, providing a simple $T^{-1/2}$ temperature dependence that is easily incorporated into a modified Arrhenius formula (Eq. 2).

For exothermic reactions, the above collisional rates are taken as the reaction rates. For endothermic reactions, the difference in proton affinities of the reactant and product neutrals is used as an activation energy (γ) in Eq. (2), but the same collisional rate approach is otherwise retained, manifesting in the α and β coefficients; see Table 4 for selected examples.

3 Results

The description of model results presented here concentrates primarily on nitrogen-bearing species; these are the molecules most strongly affected by the changes made to the chemical networks. Further, since all of the additional reactions are gas-phase processes, a particular emphasis is placed on the Stage 2 evolution of the chemistry, during which the thermal desorption of dust-grain ice mantles occurs and gas-phase destruction processes for COMs become important. The chemistry of Stage 1 is described in detail by G22, but a basic description may be found immediately below. To provide a general picture of the behaviour of the different chemical network setups in Stage 2, the main focus is placed on the *medium* warm-up timescale models.
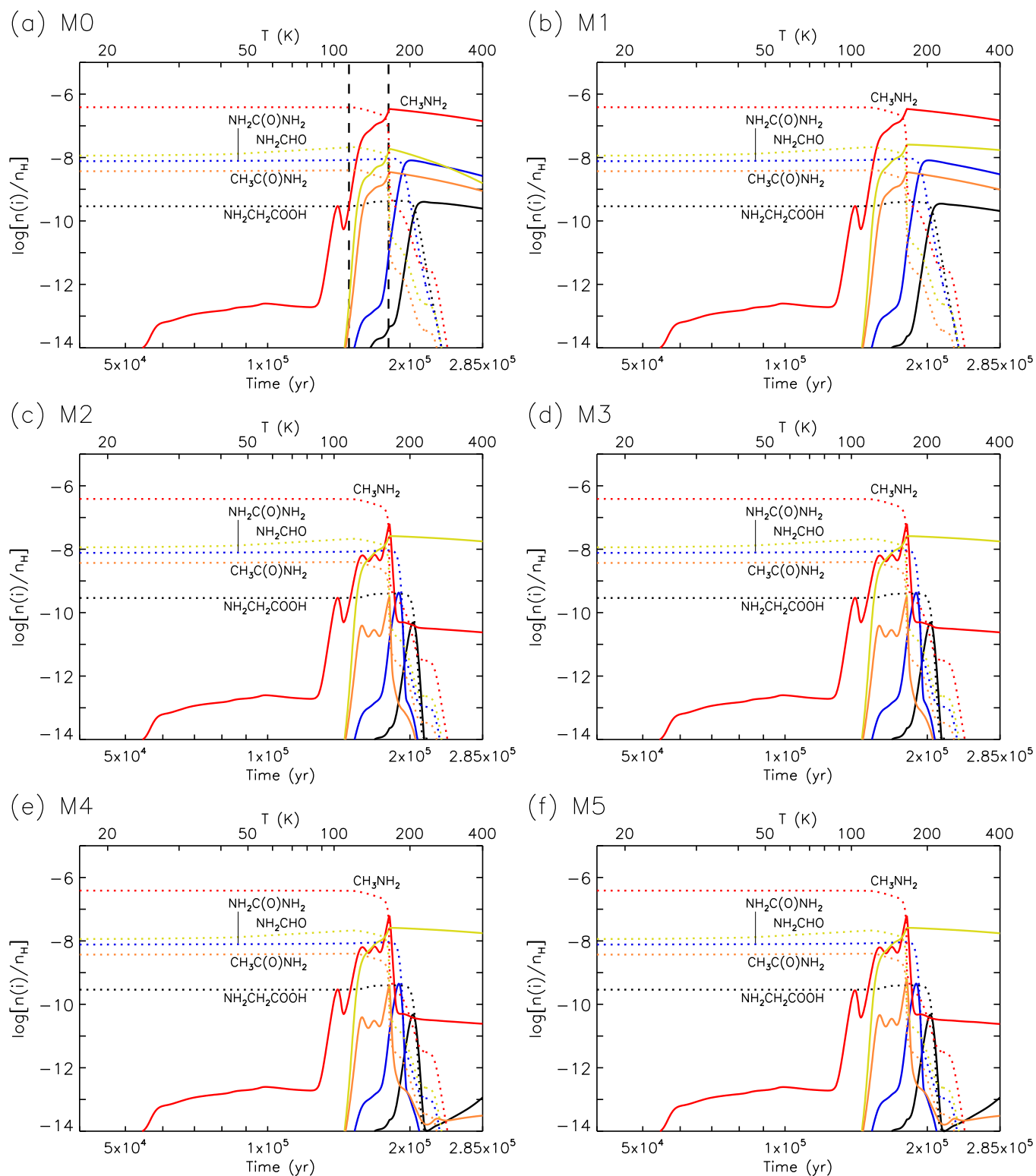
Fig. 1 Abundances with respect to total hydrogen of selected N-bearing species, for the different proton-transfer model setups using the *medium* warm-up timescale. Solid lines indicate gas-phase abundances. Dotted lines of the same colour indicate the same species on the dust grains. Vertical dashed lines in panel (a) indicate the period when substantial thermal desorption of water is occurring.

3.1 Stage 1 – collapse

During Stage 1, which simulates the gradual collapse from diffuse gas to a dense core, chemistry nevertheless occurs in both the gas phase and on the grains. Ice build-up on the grains occurs largely toward the end of Stage 1, when the gas density becomes highest. This coincides also with an increased visual extinction (diminution of the external UV field), resulting in low dust temperatures (minimum 8 K). The majority of the ice is composed of water, with substantial amounts of CO, CO_2, CH_4, NH_3, H_2CO and CH_3OH also present, as would be expected from interstellar ice observations. Much of this chemistry is driven by diffusive addition reactions of atomic H with atoms and simple radicals, all ultimately derived from the gas phase. Table 5 shows the final abundances of the main ice components and a selection of COMs on the grains at the end of Stage 1 for model M1. Since the chemical networks of models M0 – M5 vary only in the proton transfer reactions that become critical during Stage 2, there are no meaningful differences in ice composition achieved in Stage 1 between the different models.

Data for a selection of COMs and/or N-bearing species in the grain-surface ices are also shown in Table 5. The abundances of COMs in the gas phase during Stage 1 are relatively small and do not, in general, contribute significantly to the abundances studied in the "hot" Stage 2; however, a few COMs, such as dimethyl ether (CH_3OCH_3) have effective gas-phase production mechanisms in the model that can become dominant during Stage 2.

Various O-bearing COMs, including methyl formate ($HCOOCH_3$), are produced on the grains most strongly toward the end of Stage 1, through nondiffusive surface reactions between radicals related to the hydrogenation of CO to methanol. For methyl formate in particular, this occurs when the HCO radical is formed in proximity to the CH_3O radical (and *vice versa*), leading to immediate reaction. The production of the two radicals is, however, driven by H diffusion on the grain/ice surface.

Methylamine, on the other hand, is mostly produced very early on in Stage 1, when the ices are relatively thin but the visual extinction experienced is still low (around 3 mag.). This allows external UV photons to dissociate methane and ammonia in the bulk ice, allowing the resultant radicals to react to form CH_3NH_2. Ethylamine is formed in a similar way. Just such a mechanism also dominates the formation of glycine in the ice, based on the photodissociation of ammonia and acetic acid (CH_3COOH).

The very large solid-phase abundances of COMs produced on the grains during Stage 1 are retained through Stage 2, and may be enhanced at early periods in Stage 2 while still present on the grains, mainly through bulk-ice UV photolysis driven by the local UV field that is produced by cosmic ray collisions with gas-phase H_2. Table 22 of G22 indicates the periods in the model (as a function of temperature regime) when each molecule is formed. The N-bearing COMs of most interest here (those with large PA) are produced on the grains, mainly during Stage 1, in the G22 models and in all those presented here.

3.2 Stage 2 – warm-up

Fig. 1 shows results for selected nitrogen-bearing molecules during Stage 2 (warm-up) for model setups M0 – M5, using the *medium* warm-up timescale. In each figure panel, the chemical abundances of the molecules are presented with respect to total hydrogen, i.e. $n(H) + 2n(H_2)$, and as a function of time in years. Time is plotted logarithmically on the lower axis, with the coupled gas and dust temperature shown along the top. Each plot begins a little way into the Stage 2 evolution, but no major change occurs before this time for the species shown. The gas-phase abundance of each molecule is indicated by a solid line, while the total amount of the same molecule on the grain surface (i.e. surface layer + bulk ice) is shown with a dotted line of the same colour.

During this Stage 2 evolution, the dust gradually warms up, such that each of the five species shown, which originate primarily from grain-surface chemistry during Stage 1, are gradually desorbed. Due to the use of a three-phase approach in the *MAGICKAL* code, the surface layer of predominantly water ice may act to trap the more volatile species in the bulk ice until water itself begins to desorb strongly, although partial loss of volatiles can occur at lower temperatures. When water desorption begins in earnest (not shown directly in these figures – see G22), at ~114 K, molecules with surface binding energies comparable to or lower than that of water may also begin to desorb more strongly, usually reaching gas-phase peak abundances sometime between this initial release and the moment when most of the previously solid water has desorbed into the gas, which occurs by ~164 K (G22). These two key temperatures are marked with vertical dashed lines in Fig. 1, panel (a). In both panels (a) and (b), corresponding to models M0 and M1, this behaviour is observed for methylamine (CH_3NH_2), formamide (NH_2CHO) and acetamide ($CH_3C(O)NH_2$). Each of these species has a slightly higher binding energy than water, but their own rapid release begins not long after water, which also encourages the faster release of water itself, so that water and all of these species tend to reach their gas-phase peak abundances at a similar point.

Urea ($NH_2C(O)NH_2$) and glycine (NH_2CH_2COOH) achieve their gas-phase peak values at later times, and thus higher temperatures; their stronger binding energies mean that they desorb primarily after most water has left the grains, although they may themselves act to trap a small amount of water (and other species of lower binding energy) beyond its own natural desorption temperature. Due to this trapping effect, involving multiple species each with somewhat different binding energies, the desorption behaviour of COMs during the warm-up stage is complex.

Panel (a) demonstrates the degradation of gas-phase abundances without the inclusion of any proton transfer reactions from COMs directly to ammonia (model M0), once the molecules have been released from the grains; this gradual decay is caused mainly by PT from small ions and subsequent electronic dissociative recombination. Panel (b) shows the effect of the inclusion of PT from the protonated forms of lower-PA molecules to ammonia (model M1) to enhance the gas-phase lifetimes of certain species; the effect is seen only for NH_2CHO in panel (b), as the other molecules have proton affinities greater than $PA(NH_3)$, meaning
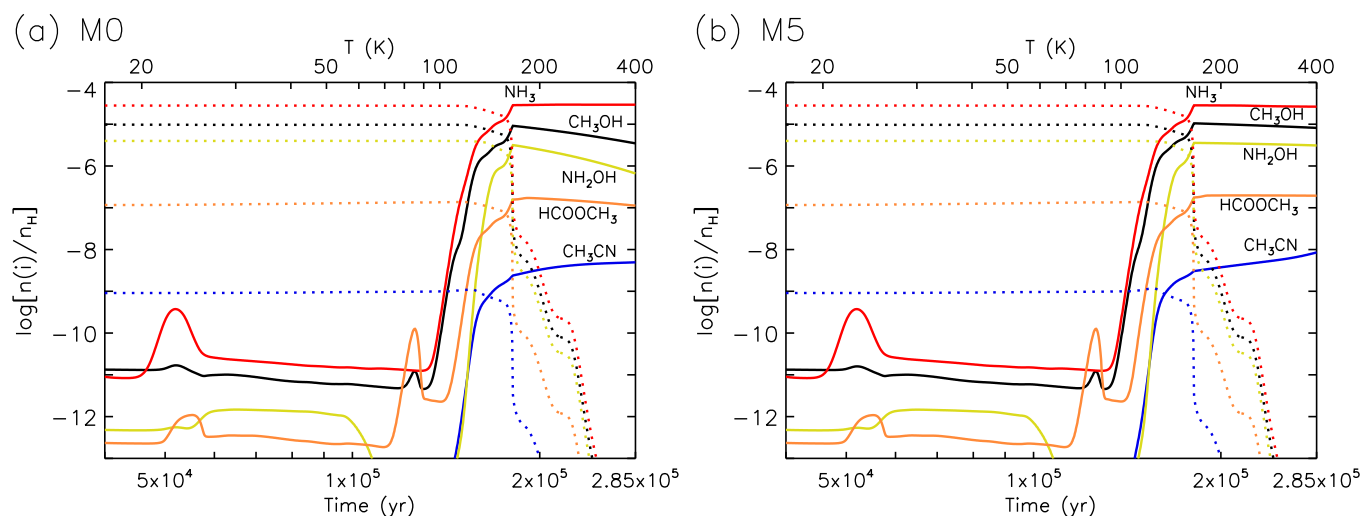
Fig. 2 Abundances with respect to total hydrogen of selected O- and N-bearing species, for the different proton-transfer model setups using the *medium* warm-up timescale. Solid lines indicate gas-phase abundances. Dotted lines of the same colour indicate the same species on the dust grains.
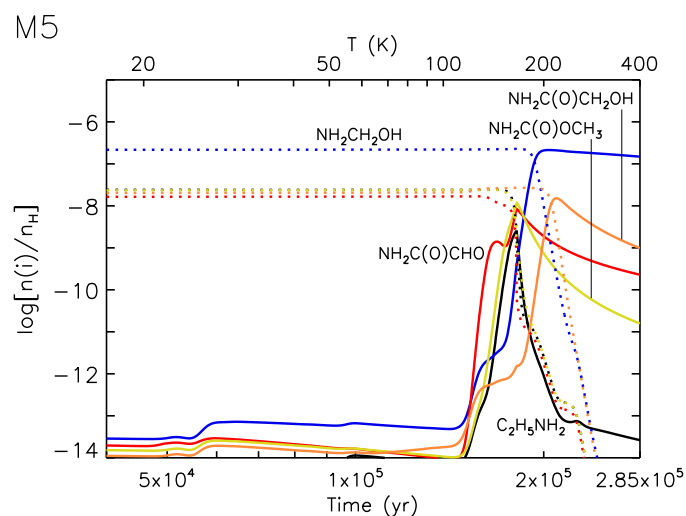
Fig. 3 Abundances with respect to total hydrogen of selected N-bearing species, for the M5 model setup using the *medium* warm-up timescale. Solid lines indicate gas-phase abundances. Dotted lines of the same colour indicate the same species on the dust grains.

that no such reactions are included for them in M1.

Fig. 1, panel (c), shows the influence of the inclusion of PT reactions from protonated ammonia to COMs with very high proton affinities; while NH_2CHO is unaffected, the other four species, each with a large PA, readily accepts a proton from NH_4^+, whose own production rates are enhanced due to the transfer from protonated molecules with PA lower than $PA(NH_3)$. The effect is dramatic, reducing both the peak abundances achieved and the lifetimes of those high-PA COMs. Although less obvious in panel (c), each of the molecules shown does reach a somewhat stable post-desorption abundance (as in e.g. panel a), but at a much lower absolute value; CH_3NH_2, for example, falls rapidly by around 3 orders of magnitude from its peak down to a more stable value of a few $10^{-11}n_H$.

In Fig. 1, panel (c), the desorption behaviour of methylamine

and acetamide in particular appear more complex than in panels (a) and (b), achieving multiple local peak abundances over the temperature range at which water is desorbing (shown as vertical dashed lines in panel a). This effect is caused by the combination of (i) multiple stages of faster/slower desorption related to the evolving ice-surface composition, and (ii) the more rapid destruction induced by the new PT reactions, which pulls down the peak gas-phase abundance achieved with each desorption spike. Note that ammonia itself is being released form the grains at this time, sufficient to have an immediate influence on proton transfer. The effect is an overall more stable abundance for these two COMs *during the desorption period itself*, although the final gas-phase peak is still achieved late in the desorption period. For methyl amine, a fractional abundance of a little less than $10^{-8}n_H$ is maintained through this period, before the late peak and precipitous drop occur.

Panels (d) – (f) in In Fig. 1 show the results for models M3 – M5. Differences between these models are much smaller and are difficult to discern from the figures, aside from the slight upticks in the late-time abundances of glycine and acetamide in models M4 and M5. These are caused by the addition of the backward (endothermic) proton transfer reactions from protonated glycine and acetamide to ammonia. Although the reaction rates are substantially less than the collisional rates (e.g. a reaction efficiency of $\sim 10^{-6}$ for protonated glycine to react with NH_3 at 300 K), the abundance of ammonia is high enough to make these reactions competitive with electronic recombination, given high enough temperatures. The absolute abundances of these COMs are nevertheless very small when the backward reactions become more efficient.

In Fig. 2, panel (a), abundances are shown for a selection of other species, including the COMs methanol (CH_3OH), methyl formate ($HCOOCH_3$) and methyl cyanide (CH_3CN). Panel (b) in the same figure shows those same species for model M5, which is chosen as representative of the behaviour in all of models M1 – M5 (models M2 – M5 vary little from M1 for these species).
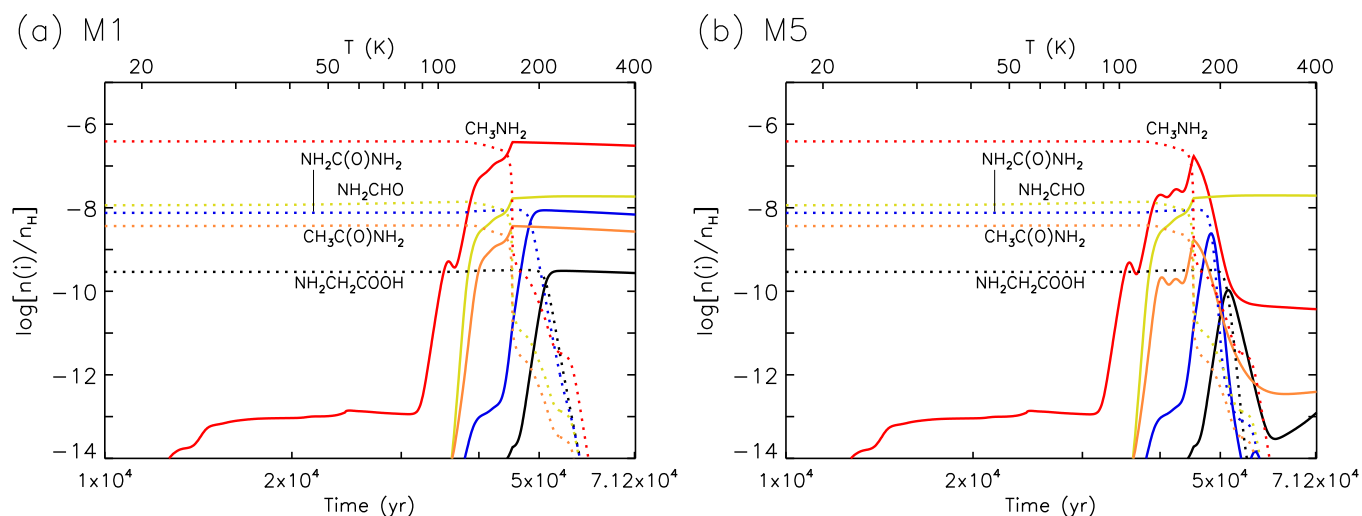
Fig. 4 Abundances with respect to total hydrogen of selected N-bearing species, for the different proton-transfer model setups using the *fast* warm-up timescale. Solid lines indicate gas-phase abundances. Dotted lines of the same colour indicate the same species on the dust grains.

The abundances of the three COMs, as well as hydroxylamine (NH$_2$OH), are seen to be enhanced in the gas-phase to a greater or lesser extent; the most obvious effect is a slow-down in their decay. The behaviour of ammonia is seen to be little affected, reaching only a marginally lower abundance at the very end of the simulation in Fig. 2, panel (b). CH$_3$CN in the G22 models (generally) is formed mainly in the gas phase; the effect of the introduction of a PT reaction from protonated methyl cyanide to ammonia is to produce an even greater rise at late times.

Fig. 3 shows model M5 abundances for some of the remaining NH$_2$-bearing molecules shown in Table 1, some of which have greater PA than ammonia. For ethylamine (C$_2$H$_5$NH$_2$), with one of the highest PA values, the gas-phase abundance peak is brief, due to reactions with NH$_4^+$. For methanolamine (NH$_2$CH$_2$OH), whose PA is estimated here to be less than PA(NH$_3$), a strong gas-phase abundance is maintained following desorption. For glycolamide (NH$_2$C(O)CH$_2$OH) and two other structures for which we have made estimates of the PA (NH$_2$C(O)OCH$_3$ and NH$_2$C(O)CHO), the backward reactions allowing PT back to ammonia are relatively efficient, lessening the effect of PT in the forward direction. The latter three species have not been detected in the ISM so far, and are included in the network mainly for completeness. The uncertain nature of their PA estimates leaves their gas-phase behaviour also rather unreliable.

The models were also run for the *fast* and *slow* warm-up timescales. Limited results for these two cases are shown in Figs. 4 and 5. Only the results for models M1 and M5 are shown; the behaviour of the M2 – M4 models is largely in line with that described above for the *medium* timescale models. With the shorter warm-up timescale, the effect of the enhanced gas-phase destruction mechanisms is somewhat more muted as a function of temperature, due to the shorter times spent in the gas phase. More specifically, the peak abundances achieved in the gas phase are somewhat higher in the *fast* model, due to the more rapid injection of material into the gas phase, versus the gas-phase destruction timescale. This is true throughout the main ice desorp-

tion period (114 – 164 K) for those species which undergo multiple desorption spikes. For the late-peaking glycine and urea, peak gas-phase values achieved in the *fast* model are crudely around an order of magnitude higher than in the *medium* timescale case, when comparing between model M5 runs. A similar relationship holds in reverse, when comparing the *slow* with the *medium* warm-up timescales for model M5.

Tables 6, 7 and 8 show instantaneous abundances obtained for a selection of molecules in models M0, M1, M3 and M5, corresponding to the *medium*, *fast* and *slow* warm-up timescales, respectively. Results for models M2 and M4 are omitted due to their similarity to those of models M3 and M5, respectively. In the top half of each table are shown molecules with proton affinities greater than PA(NH$_3$), for which some substantial change in results might be expected with the addition of the new PT reactions. Only model M5 includes new reactions directly involving production or destruction of NaOH, the species with the highest PA in the model. The lower half of each table shows molecules that are either commonly observed toward hot star-forming cores or those that are of particular interest, such as NH$_2$OH. The first column of abundance data in each table shows the peak ice abundance achieved for that species during Stage 2; in most cases, the majority of the gas-phase abundance of the molecule originates on the grains. This data therefore provides a reference point for the degree of destruction suffered by each molecule. This peak ice abundance is essentially the same in each of models M0 – M5, as only the gas-phase reactions vary between models, although values vary between different warm-up timescales, due to the different amounts of thermal and/or UV processing experienced by the ice mantles prior to desorption. For each model and molecule, a peak gas-phase value is provided, along with the final gas-phase value achieved at the end of the model, corresponding to a temperature of 400 K.

As seen in the figures, the most drastic changes occur with the introduction of proton transfer from NH$_4^+$ to high-PA COMs in model M2 (whose results are very similar to the values shown for
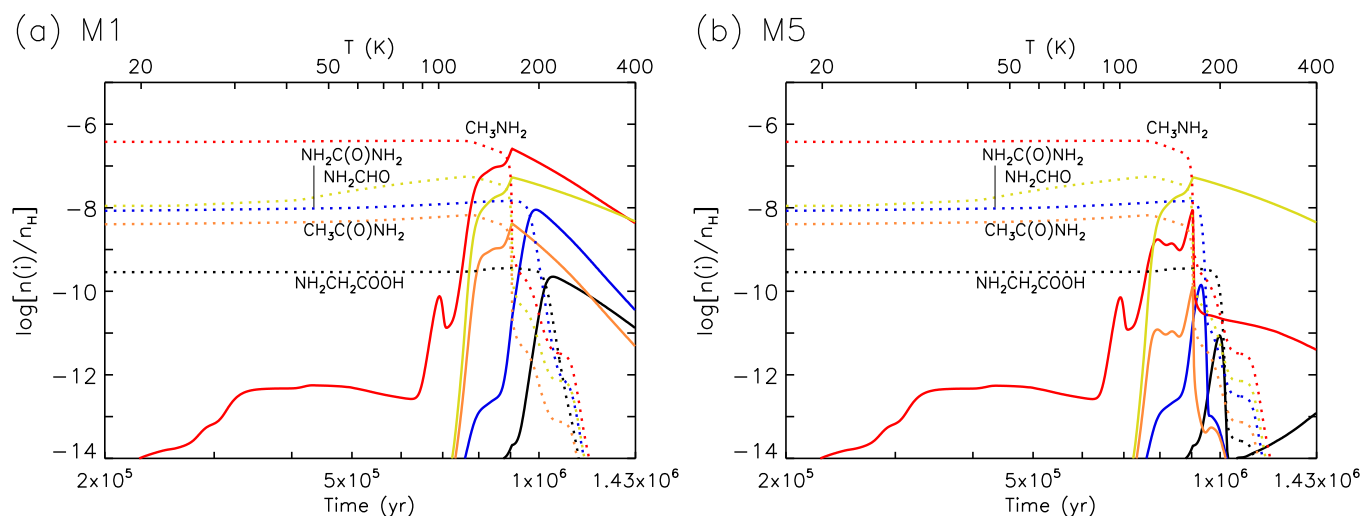
Fig. 5 Abundances with respect to total hydrogen of selected N-bearing species, for the different proton-transfer model setups using the *slow* warm-up timescale. Solid lines indicate gas-phase abundances. Dotted lines of the same colour indicate the same species on the dust grains.

M3). Peak gas-phase abundances for those NH_2 group-bearing COMs, of which five are presented in the table, fall solidly by a factor of a few to more than an order of magnitude between M1 and M3, dependent on warm-up timescale, but the later gas-phase destruction is yet more drastic, as evidenced by the final abundances.

The effects on the important methanol molecule are noticeable but not very substantial for the purposes of astronomical comparison; it nevertheless undergoes a slight peak enhancement, and a longer survival time against gas-phase destruction, as with other COMs of PA less than that of NH_3, such as the commonly observed O-bearing COMs methyl formate and dimethyl ether. The effects on NH_3 itself are also seen to be modest. Hydroxylamine shows only minor peak abundance increases due to the new reactions, while enjoying the same major increases in longevity, especially in the *slow* warm-up model. It also remains unaffected by its inclusion in the more comprehensive reaction set of model M5.

4 Discussion

While not every addition to the chemical networks implemented here shows an important effect, the inclusion of proton transfer from NH_4^+ to NH_2-bearing COMs has a drastic influence on the abundances of the latter when combined also with the enhanced proton transfer from low-PA COMs to NH_3. Peak abundances are lowered by around an order of magnitude in these models, when comparing between like warm-up timescales. This effect was suggested as a possible explanation for the overproduction of urea in earlier chemical models, when compared with its detected abundances toward the Galactic Center hot core source Sgr B2(N1).[9] Although G22 included a far more comprehensive treatment for surface and ice chemistry than those models, the same overproduction was also found by G22. The observed abundance of urea toward position Sgr B2(N1S)[9] was determined to be 2.7×10^{16} cm^{-2}, yielding a ratio $NH_2CHO:NH_2CONH_2$ of $\sim$107, while the M1 models (the same as G22) result in a value of 6, at best, when comparing peak formamide with peak urea

values. Meanwhile, the new M5 models produce ratios 8.2, 58 and 380 for the *fast*, *medium* and *slow* models respectively (using data from Tables 6–8). G22 showed that the *slow* warm-up timescales tend to produce the best overall match with higher-mass sources, so the new models may be within a factor of a few of reproducing the observed urea values, using this crude peak-to-peak comparison.

It is interesting also that the urea observations toward Sgr B2(N2), which is in the same collection of high-mass star-forming cores as core N1, yielded no detection of urea at all, with a lower limit for the ratio $NH_2CHO:NH_2CONH_2$ of $\sim$1100. While this is not ideally consistent with the comparison of peak model abundance values, it would be far more consistent with the abundances reached either before urea is desorbed in the models, or after. The M5 abundance peak is relatively brief, indicating that the successful detection of urea may be dependent on the observed source or position being in just the right stage of evolution. At too low a temperature, urea would still be in the solid phase, while following desorption it would be short-lived.

The sharply peaked behaviour found for urea therefore makes a very meaningful comparison between these models and the observations rather tricky; the models are physically simple, containing no explicit spatial information. Direct comparison would require a chemical model with spatial structure. However, the peak-to-peak abundance ratios obtained from the models may provide at least a good best-case limit for observational detection of urea toward other sources.

Acetamide ($CH_3C(O)NH_2$), however, while still suffering from rapid gas-phase destruction, manages to maintain a substantial abundance for a more significant period of time. Like methylamine, its gradual desorption along with water over a range of temperatures means that it could potentially be more easily observed at hot-core temperatures up to around 160 K or so. Acetamide was indeed detected toward both sources Sgr B2(N1) and B2(N2).[9] However, it is less abundant in the models than would be expected from the observed ratio with NH_2CHO.

Table 6 Selected results from the *medium* warm-up timescale model runs. For each model, the peak abundance of the molecule achieved in the gas phase is provided along with the final value. For each molecule, the peak ice-mantle abundance value is also shown, which does not vary significantly between models M0–M5, assuming the same warm-up timescale is adopted. Chemical species in the upper half of the table are those that might be expected to demonstrate substantial variations in abundance between models M1–M5, and all have proton affinity greater than PA(NH$_3$). The lower half of the table shows commonly observed or otherwise noteworthy species. Notation $a(-b)$ indicates $a \times 10^{-b}$.

| Molecule | Fractional abundance, $n(i)/n_{\mathrm{H}}$ | | | | | | | | |
| | | M0 | | M1 | | M3 | | M5 | |
	Peak Ice	Peak Gas	Final Gas	Peak Gas	Final Gas	Peak Gas	Final Gas	Peak Gas	Final Gas
CH$_3$NH$_2$	3.89(-7)	3.39(-7)	1.40(-7)	3.39(-7)	1.48(-7)	6.33(-8)	2.39(-11)	6.16(-8)	2.40(-11)
C$_2$H$_5$NH$_2$	2.42(-8)	2.07(-08)	9.90(-9)	2.08(-8)	1.04(-8)	4.82(-9)	4.58(-14)	2.46(-9)	2.63(-14)
CH$_3$C(O)NH$_2$	3.91(-9)	3.48(-9)	8.78(-10)	3.45(-9)	9.78(-10)	2.98(-10)	8.70(-16)	6.40(-10)	3.05(-14)
NH$_2$C(O)NH$_2$	8.28(-9)	8.13(-9)	2.62(-9)	8.15(-9)	2.95(-9)	4.25(-10)	1.29(-19)	4.49(-10)	1.18(-18)
NH$_2$CH$_2$COOH	2.92(-10)	4.01(-10)	2.45(-10)	3.51(-10)	2.07(-10)	4.85(-11)	2.72(-15)	4.67(-11)	1.16(-13)
NaOH	1.65(-13)	2.47(-11)	2.47(-11)	2.48(-11)	2.48(-11)	2.47(-11)	2.47(-11)	7.26(-12)	3.66(-12)
CH$_3$OH	9.64(-6)	9.14(-6)	3.48(-6)	1.05(-5)	8.15(-6)	1.05(-5)	8.16(-6)	1.05(-6)	8.16(-6)
CH$_3$CN	9.53(-10)	4.94(-9)	4.94(-9)	8.20(-9)	8.20(-9)	8.53(-9)	8.53(-9)	8.51(-9)	8.51(-9)
NH$_3$	2.81(-5)	2.95(-5)	2.93(-5)	2.80(-5)	2.60(-5)	2.83(-5)	2.61(-5)	2.83(-5)	2.62(-5)
NH$_2$CHO	2.13(-8)	1.87(-8)	1.55(-9)	2.55(-8)	1.72(-8)	2.58(-8)	1.76(-8)	2.58(-8)	1.74(-8)
NH$_2$OH	3.98(-6)	3.15(-6)	6.62(-7)	3.58(-6)	3.15(-6)	3.56(-6)	3.13(-6)	3.57(-6)	3.10(-6)
HCOOCH$_3$	1.37(-7)	1.71(-7)	1.12(-7)	1.98(-7)	1.94(-7)	1.97(-7)	1.94(-7)	1.97(-7)	1.94(-7)
CH$_3$OCH$_3$	1.06(-7)	1.48(-7)	1.45(-7)	1.77(-7)	1.77(-7)	1.70(-7)	1.70(-7)	1.69(-7)	1.69(-7)

Table 7 Selected results from the *fast* warm-up timescale model runs; see Table 6 for details.

| Molecule | Fractional abundance, $n(i)/n_{\mathrm{H}}$ | | | | | | | | |
| | | M0 | | M1 | | M3 | | M5 | |
	Peak Ice	Peak Gas	Final Gas	Peak Gas	Final Gas	Peak Gas	Final Gas	Peak Gas	Final Gas
CH$_3$NH$_2$	3.89(-7)	3.73(-7)	3.03(-7)	3.73(-7)	3.05(-7)	1.74(-7)	3.72(-11)	1.71(-7)	3.73(-11)
C$_2$H$_5$NH$_2$	2.42(-8)	1.48(-8)	1.28(-8)	1.48(-8)	1.28(-8)	8.51(-9)	4.04(-12)	5.39(-9)	3.35(-12)
CH$_3$C(O)NH$_2$	3.68(-9)	3.68(-9)	2.69(-9)	3.64(-9)	2.68(-9)	1.09(-9)	1.23(-14)	1.70(-9)	3.93(-13)
NH$_2$C(O)NH$_2$	7.62(-9)	8.72(-9)	6.83(-9)	8.70(-9)	6.86(-9)	1.95(-9)	1.98(-18)	2.41(-9)	1.96(-17)
NH$_2$CH$_2$COOH	2.92(-10)	3.25(-10)	3.06(-10)	3.09(-10)	2.73(-10)	1.16(-10)	2.93(-15)	1.07(-10)	1.24(-13)
NaOH	1.65(-13)	6.60(-12)	6.60(-12)	6.63(-12)	6.63(-12)	6.62(-12)	6.62(-12)	2.90(-12)	2.82(-12)
CH$_3$OH	9.61(-6)	1.04(-5)	8.29(-6)	1.08(-5)	1.02(-5)	1.08(-5)	1.02(-5)	1.08(-5)	1.02(-5)
CH$_3$CN	9.04(-10)	2.21(-9)	2.21(-9)	1.70(-9)	1.70(-9)	1.79(-9)	1.79(-9)	1.79(-9)	1.79(-9)
NH$_3$	2.81(-5)	2.88(-5)	2.88(-5)	2.82(-5)	2.76(-5)	2.85(-5)	2.79(-5)	2.85(-5)	2.79(-5)
NH$_2$CHO	1.39(-8)	1.51(-8)	1.08(-8)	1.88(-8)	1.85(-8)	2.02(-8)	2.00(-8)	1.97(-8)	1.95(-8)
NH$_2$OH	3.95(-6)	3.73(-6)	2.70(-6)	3.89(-6)	3.78(-6)	3.87(-6)	3.76(-6)	3.87(-6)	3.75(-6)
HCOOCH$_3$	1.20(-7)	1.75(-7)	1.66(-7)	1.88(-7)	1.88(-7)	1.89(-7)	1.88(-7)	1.88(-7)	1.88(-7)
CH$_3$OCH$_3$	8.77(-8)	1.16(-7)	1.16(-7)	1.12(-7)	1.12(-7)	1.10(-7)	1.10(-7)	1.10(-7)	1.10(-7)

Table 8 Selected results from the *slow* warm-up timescale model runs; see Table 6 for details.

| Molecule | Fractional abundance, $n(i)/n_{\mathrm{H}}$ | | | | | | | | |
| | | M0 | | M1 | | M3 | | M5 | |
	Peak Ice	Peak Gas	Final Gas	Peak Gas	Final Gas	Peak Gas	Final Gas	Peak Gas	Final Gas
CH$_3$NH$_2$	4.00(-7)	2.48(-7)	2.60(-9)	2.57(-7)	4.30(-9)	9.22(-9)	4.91(-12)	9.01(-9)	3.98(-12)
C$_2$H$_5$NH$_2$	2.42(-8)	1.81(-8)	3.13(-10)	1.82(-8)	4.20(-10)	6.88(-10)	4.79(-19)	5.22(-10)	3.77(-19)
CH$_3$C(O)NH$_2$	6.51(-9)	4.03(-9)	2.10(-12)	4.16(-9)	4.85(-12)	7.30(-11)	8.68(-20)	1.30(-10)	1.50(-18)
NH$_2$C(O)NH$_2$	1.29(-8)	8.63(-9)	1.68(-11)	8.96(-9)	3.56(-11)	1.37(-10)	9.61(-22)	1.41(-10)	3.98(-21)
NH$_2$CH$_2$COOH	2.92(-10)	2.54(-10)	1.26(-11)	2.23(-10)	1.33(-11)	8.87(-12)	2.97(-15)	8.75(-12)	1.21(-13)
NaOH	1.65(-13)	1.14(-10)	1.14(-10)	1.13(-10)	1.13(-10)	1.12(-10)	1.12(-10)	7.55(-12)	2.01(-12)
CH$_3$OH	9.59(-6)	5.34(-6)	9.57(-8)	8.31(-6)	2.40(-6)	8.32(-6)	2.36(-6)	8.32(-6)	2.37(-6)
CH$_3$CN	1.68(-9)	1.05(-8)	7.55(-9)	7.04(-8)	7.04(-8)	7.08(-8)	7.08(-8)	7.06(-8)	7.06(-8)
NH$_3$	2.81(-5)	2.98(-5)	1.52(-5)	2.71(-5)	1.27(-5)	2.74(-5)	1.24(-5)	2.74(-5)	1.25(-5)
NH$_2$CHO	5.54(-8)	2.63(-8)	1.02(-13)	5.32(-8)	4.71(-9)	5.32(-8)	4.67(-9)	5.32(-8)	4.45(-9)
NH$_2$OH	4.13(-6)	1.87(-6)	2.36(-10)	2.92(-6)	1.51(-6)	2.89(-6)	1.49(-6)	2.90(-6)	1.37(-6)
HCOOCH$_3$	1.73(-7)	1.44(-7)	1.10(-8)	2.51(-7)	2.32(-7)	2.49(-7)	2.29(-7)	2.49(-7)	2.29(-7)
CH$_3$OCH$_3$	1.60(-7)	1.44(-7)	1.84(-8)	2.18(-7)	1.73(-7)	2.11(-7)	1.84(-7)	2.11(-7)	1.82(-7)

Methylamine (CH_3NH_2) shows a similar extended lifetime in the gas phase during its gradual desorption, followed by a brief peak, then a precipitous decline. Recent observations toward sources in the star-forming region NGC 6334I indicate[8] a CH_3NH_2:NH_2CHO ratio of at least 8.2, with some lines of sight producing upper limits greater than 60. Values as high as the latter are hard to reproduce with the models, although the ratio hovers around 10 in the M5 *fast* model during the extended period of desorption from 114–164 K (a ratio around unity is found for the *medium* model). The original M0/M1 models in fact reproduced CH_3NH_2 in NGC 6334I rather well, over a wider range of temperatures. But for a species with as high a proton affinity as methylamine, the existence of an effective protonation mechanism with ammonia and various other species seems hard to avoid. Based on the highest temperature (>200 K or so) abundances for model M5, the match with observations would appear very poor. This also presents a conundrum as the observational best-fit excitation temperatures for CH_3NH_2 toward NGC 6334I are greater than 200 K, and as high as 340±60 K.

However, it may also be pertinent that methylamine has not been observed very frequently in the ISM until recently; furthermore, for the few other sources in which it has been observed, its abundance ratio with NH_2CHO is substantially lower than in NGC 6334I,[8] with a maximum around 3. It was not detected toward the well-known hot corino source IRAS 16293-2422, with an upper limit with respect to NH_2CHO of 0.053.[47,48] The abundances found toward NGC 6334I may therefore be exceptional.

The origins of methylamine in the model, along with several other NH_2-bearing species including ethylamine ($C_2H_5NH_2$) are also slightly unusual. CH_3NH_2 is formed mainly through photolysis in the early dust-grain ices, driven by external UV that penetrates the initially low visual extinction. It is unclear whether this is an accurate depiction of the chemical behaviour throughout a hot core, or whether such an effect would be highly localized to the more spatially extreme parts of the young core. If such a mechanism is indeed dominant, however, it would result in such molecules being most prevalent in the deepest layers of the ice. These might presumably be preserved to even higher temperatures than the present models are capable of reproducing, via trapping by species with yet higher binding energies; three-phase chemical models cannot distinguish between individual layers within the bulk ice. Such an effect would be perhaps more in agreement with the high excitation temperatures determined for methylamine toward NGC 6334I.

Glycine in these models is further diminished by the additional gas-phase destruction mechanisms, so that its already meagre fractional abundances appear to fall rapidly beneath any hope of detectability. It seems, then, that the new models would make it even less likely that the long-sought detection of glycine in the ISM might be forthcoming.

Hydroxylamine (NH_2OH) has been problematic for the models for a long time; it is strongly overproduced, while until very recently it had never been detected in the ISM at all.[24] Although it is present toward the quiescent Galactic Center cloud G+0.693,[12] it has not yet been detected toward a star-forming region. The models presented here indicate that whatever the cause of the

overproduction – by several orders of magnitude – it is unlikely to be related to proton transfer reactions. In spite of the NH_2-group borne by hydroxylamine, its PA is substantially lower than that of ammonia. The overproduction of NH_2OH in the models may well be due to inappropriate assumptions about the efficiency of its formation from NO and HNO on grain surfaces.

Toward the G+0.693 source, a wealth of NH_2-bearing molecules has been detected, including some molecules with very large proton affinities, such as ethylamine. It is natural to ask whether this source is unique in its molecular abundances (as compared with star-forming sources), or only in the means of the delivery of those molecules to the gas phase (i.e. shock heating or sputtering, versus the assumed thermal desorption in the present hot-core models). It is notable that the gas number density in G+0.693 is estimated to be of the order of 10^4–10^5 cm^{-3},[49] i.e. three to four orders of magnitude greater than in these models, meaning that the action of proton transfer reactions would be correspondingly slower, producing greater peak abundances and much longer lifetimes for affected molecules. The rapid ejection of COMs from the grains following a shock would also help to keep abundances high, while potentially also preserving the relative abundances of the ice constituents more fully, assuming that the chemistry during the shock did not have a strong effect. It seems likely, then, that the PT mechanisms that are so destructive for certain species in hot cores may have a far less pronounced effect in a quiescent COM-rich source, and may provide an additional point of divergence between G+0.693 and the more typical environments in which COMs are detected.

The inclusion of endothermic reactions in the networks of models M4 and M5 is partly intended to avoid the situation where exothermic reactions of very modest reaction enthalpies would have an outsized influence on the chemistry even at high temperatures, at which the reverse process might be competitive. However, the overall effect of their inclusion is minor, except for a few cases (e.g. Fig. 3), and the PAs of some of the species affected are only based on estimates rather than measured values, making these results less reliable. However, as seen with glycine, at high temperatures the endothermic reaction can become competitive with other processes even when the endothermicity is very large. A more complete reaction network would have to consider additional branches with alternative reaction products, giving a reaction with smaller endothermicity, which could make proton transfer the less likely outcome.

For exothermic reactions involving PT to COMs with extremely high PA values, even a reaction with H_3O^+ might be sufficiently energetic to make destruction of the COM the more likely outcome, versus the simple proton transfer assumed here. However, since these species already suffer rapid destruction in the gas phase as the result of the new PT reactions with NH_4^+ (followed by dissociative recombination), the result may not be much worse for the abundances of those molecules.

We note finally that the proton transfer reactions of protonated COMs with ammonia are important primarily because they are competitive with the electronic dissociative recombination that would otherwise lead to the destruction of the underlying molecules. Likewise, proton transfer from NH_4^+ to higher-

PA COMs is critically destructive because the resulting protonated COMs have no alternative neutralization mechanism that is sufficiently competitive with DR. However, reactions of cations with negatively charged PAHs could provide a further competing mechanism, which might potentially mitigate the more extreme outcomes of the models presented here; modeling studies have indicated that charged PAHs can have an important influence on the chemistry of dark interstellar clouds.[50]

5 Conclusions

Much focus has necessarily been placed over the years on the origins of interstellar COMs, and thus on the particular formation mechanisms involved. However, destruction mechanisms, particularly in the gas phase, are equally important in determining their observed abundances. With the inclusion of a more comprehensive network of proton-transfer reactions for COMs, a clear distinction arises between those with and without an amine group. The former will tend to have higher proton affinities, greater even than ammonia, apparently dooming them to rapid destruction following their desorption into the high-density gas-phase conditions prevalent in hot, star-forming cores. This occurs due to the strong transfer of protons from various other protonated molecules to abundant ammonia, producing NH_4^+, which then passes the protons on to those COMs of even higher proton affinity. With no competing reaction process available, due to the relatively low abundances of all the other high-proton affinity species, the resultant protonated, amine group-bearing COMs are destroyed by electronic dissociative recombination.

Methylamine (CH_3NH_2) has one of the larger proton affinities of molecules detected in such regions; this makes its substantial observed abundance in some sources difficult to explain, while being apparently consistent with its more general non-detection. Meanwhile, the recently detected hydroxylamine (NH_2OH), which is usually vastly overproduced in astrochemical models, remains unaffected by the newly added proton transfer reactions, due to its lower proton affinity.

The destructive effect on NH_2-bearing molecules is helpful in more accurately reproducing the abundance of interstellar urea in the astrochemical models. However, the extreme gas-phase destruction found in the simulations for the amino acid glycine seems further to mitigate against its possible detection in the ISM.

While NH_2-bearing molecules are strongly affected by the reactions studied here, not all nitrogenated COMs are affected in this way. Nitriles, bearing the CN-group, are commonly observed in star-forming cores and are not subject to the rapid destruction described in this work. The new chemical networks explored here also included proton transfer reactions for a number of other species that do not contain nitrogen, but which nevertheless have a very high proton affinity, i.e. C_2S, C_3O, C_3S and NaOH. While these molecules were not the focus of this study, their abundances certainly decline with the inclusion of the new reactions. However, due to their generally much lower abundances, their presence in the suite of proton transfer reactions has no major effect on the abundances of COMs.

Numerous new reactions have been tested here, especially in the M5 network. However, for the completion of existing astro-chemical networks (that include high-PA COMs) used by other astrochemical modelers, it is reasonable to assume that only the exothermic reactions involving NH_3, NH_4^+, CH_3OH and $CH_3OH_2^+$ (model M3) are necessary to obtain a fairly accurate outcome.

In comparisons of hot core models with observations, it has been convenient to use the peak abundances of various species as representative of the chemical composition of a hot core more broadly. The fidelity of this approach has relied on the gas-phase abundances of the various COMs reamaining relatively stable with respect to each other over long periods of time, following their arrival in the gas phase (such as in models M0 and M1). Clearly, this requirement is not fulfilled for COMs with proton affinities greater than that of ammonia. Explaining the observed abundances of these species using simple models that do not account for dynamic physical conditions and molecular spatial distributions during the hot period will be challenging.

Author Contributions

RTG calculated chemical reaction rates, ran astrochemical models, and contributed to the article text. EH advised on chemical reaction rates and contributed to the article text.

Conflicts of interest

There are no conflicts to declare.

Acknowledgements

Notes and references

1 E. Herbst and E. F. van Dishoeck, *Ann. Rev. Astron. Astrophys.*, 2009, **47**, 427–480.

2 R. D. Brown, J. G. Crofts, F. F. Gardner, P. D. Godfrey, B. J. Robinson and J. B. Whiteoak, *Astrophys. J. Lett.*, 1975, **197**, L29–L31.

3 L. E. Snyder, D. Buhl, P. R. Schwartz, F. O. Clark, D. R. Johnson, F. J. Lovas and P. T. Giguere, *Astrophys. J. Lett.*, 1974, **191**, L79.

4 I. Jiménez-Serra, L. F. Rodríguez-Almeida, J. Martín-Pintado, V. M. Rivilla, M. Melosso, S. Zeng, L. Colzi, Y. Kawashima, E. Hirota, C. Puzzarini, B. Tercero, P. de Vicente, F. Rico-Villas, M. A. Requena-Torres and S. Martín, *Astron. & Astrophys.*, 2022, **663**, A181.

5 A. Belloche, R. T. Garrod, O. Zingsheim, H. S. P. Müller and K. M. Menten, *Astron. & Astrophys.*, 2022, **662**, A110.

6 N. Kaifu, M. Morimoto, K. Nagane, K. Akabane, T. Iguchi and K. Takagi, *Astrophys. J. Lett.*, 1974, **191**, L135–L137.

7 N. Fourikis, K. Takagi and M. Morimoto, *Astrophys. J. Lett.*, 1974, **191**, L139.

8 E. G. Bøgelund, B. A. McGuire, M. R. Hogerheijde, E. F. van Dishoeck and N. F. W. Ligterink, *Astron. & Astrophys.*, 2019, **624**, A82.

9 A. Belloche, R. T. Garrod, H. S. P. Müller, K. M. Menten,

I. Medvedev, J. Thomas and Z. Kisiel, *Astron. & Astrophys.*, 2019, **628**, A10.

10 S. Martín, M. A. Requena-Torres, J. Martín-Pintado and R. Mauersberger, *Astrophys. J.*, 2008, **678**, 245–254.

11 I. Jiménez-Serra, P. Caselli, J. Martín-Pintado and T. W. Hartquist, *Astron. & Astrophys.*, 2008, **482**, 549–559.

12 V. M. Rivilla, J. Martín-Pintado, I. Jiménez-Serra, S. Martín, L. F. Rodríguez-Almeida, M. A. Requena-Torres, F. Rico-Villas, S. Zeng and C. Briones, *Astrophys. J. Lett.*, 2020, **899**, L28.

13 S. Zeng, I. Jiménez-Serra, V. M. Rivilla, J. Martín-Pintado, L. F. Rodríguez-Almeida, B. Tercero, P. de Vicente, F. Rico-Villas, L. Colzi, S. Martín and M. A. Requena-Torres, *Astrophys. J. Lett.*, 2021, **920**, L27.

14 V. M. Rivilla, I. Jiménez-Serra, J. Martín-Pintado, C. Briones, L. F. Rodríguez-Almeida, F. Rico-Villas, B. Tercero, S. Zeng, L. Colzi, P. de Vicente, S. Martín and M. A. Requena-Torres, *Proceedings of the National Academy of Science*, 2021, **118**, e2101314118.

15 Y.-J. Kuan, S. B. Charnley, H.-C. Huang, W.-L. Tseng and Z. Kisiel, *Astrophys. J.*, 2003, **593**, 848–867.

16 L. E. Snyder, F. J. Lovas, J. M. Hollis, D. N. Friedel, P. R. Jewell, A. Remijan, V. V. Ilyushin, E. A. Alekseev and S. F. Dyubko, *Astrophys. J.*, 2005, **619**, 914–930.

17 M. R. Cunningham, P. A. Jones, P. D. Godfrey, D. M. Cragg, I. Bains, M. G. Burton, P. Calisse, N. H. M. Crighton, S. J. Curran, T. M. Davis, J. T. Dempsey, B. Fulton, M. G. Hidas, T. Hill, L. Kedziora-Chudczer, V. Minier, M. B. Pracy, C. Purcell, J. Shobbrook and T. Travouillon, *Mon. Not. R. Astron. Soc.*, 2007, **376**, 1201–1210.

18 P. A. Jones, M. R. Cunningham, P. D. Godfrey and D. M. Cragg, *Mon. Not. R. Astron. Soc.*, 2007, **374**, 579–589.

19 J. E. Elsila, D. P. Glavin and J. P. Dworkin, *Meteoritics & Planetary Science*, 2009, **44**, 1323–1330.

20 K. Altwegg, H. Balsiger, A. Bar-Nun, J. J. Berthelier, A. Bieler, P. Bochsler, C. Briois, U. Calmonte, M. R. Combi, H. Cottin, J. De Keyser, F. Dhooghe, B. Fiethe, S. A. Fuselier, S. Gasc, T. I. Gombosi, K. C. Hansen, M. Haessig, A. Ja ckel, E. Kopp, A. Korth, L. Le Roy, U. Mall, B. Marty, O. Mousis, T. Owen, H. Reme, M. Rubin, T. Semon, C. Y. Tzou, J. H. Waite and P. Wurz, *Science Advances*, 2016, **2**, e1600285–e1600285.

21 R. T. Garrod, *Astrophys. J.*, 2013, **765**, 60.

22 S. Ioppolo, G. Fedoseev, K. J. Chuang, H. M. Cuppen, A. R. Clements, M. Jin, R. T. Garrod, D. Qasim, V. Kofman, E. F. van Dishoeck and H. Linnartz, *Nature Astronomy*, 2021, **5**, 197–205.

23 R. T. Garrod, M. Jin, K. A. Matis, D. Jones, E. R. Willis and E. Herbst, *Astrophys. J. Supp.*, 2022, **259**, 1.

24 R. L. Pulliam, B. A. McGuire and A. J. Remijan, *Astrophys. J.*, 2012, **751**, 1.

25 J. K. Jørgensen, A. Belloche and R. T. Garrod, *Ann. Rev. Astron. Astrophys.*, 2020, **58**, 727–778.

26 R. T. Garrod, S. L. Widicus Weaver and E. Herbst, *Astrophys. J.*, 2008, **682**, 283–302.

27 W. D. Geppert, M. Hamberg, R. D. Thomas, F. Österdahl, F. Hellberg, V. Zhaunerchyk, A. Ehlerding, T. J. Millar, H. Roberts, J. Semaniak, M. A. Ugglas, A. Källberg, A. Simonsson, M. Kaminska and M. Larsson, *Faraday Discussions*, 2006, **133**, 177.

28 A. Bacmann, V. Taquet, A. Faure, C. Kahane and C. Ceccarelli, *Astron. & Astrophys.*, 2012, **541**, L12.

29 G. Fedoseev, H. M. Cuppen, S. Ioppolo, T. Lamberts and H. Linnartz, *Mon. Not. R. Astron. Soc.*, 2015, **448**, 1288–1297.

30 I. Jiménez-Serra, A. I. Vasyunin, P. Caselli, N. Marcelino, N. Billot, S. Viti, L. Testi, C. Vastel, B. Lefloch and R. Bachiller, *Astrophys. J. Lett.*, 2016, **830**, L6.

31 M. Jin and R. T. Garrod, *Astrophys. J. Supp.*, 2020, **249**, 26.

32 M. Hamberg, V. Zhaunerchyk, E. Vigren, M. Kaminska, I. Kashperka, M. Zhang, S. Trippel, F. Österdahl, M. A. Ugglas, R. D. Thomas, A. Källberg, A. Simonsson, A. Paál, J. Semaniak, M. Larsson and W. D. Geppert, *Astron. & Astrophys.*, 2010, **522**, A90.

33 E. P. Hunter and S. G. Lias, *J. Phys. Chem. Ref. Data*, 1998, **27**, 413–656.

34 X. Zeng and R. G. Cooks, *J. Phys. Chem. A*, 2002, **106**, 99309.

35 V. G. Anicich, *JPL publication*, 2003, **03-19**,.

36 V. G. Anicich, *Journal of Physical and Chemical Reference Data*, 1993, **22**, 1469–1569.

37 V. Taquet, E. S. Wirström and S. B. Charnley, *Astrophys. J.*, 2016, **821**, 46.

38 W. Y. Feng and C. Lifshitz, *J. Phys. Chem.*, 1994, **98**, 3658–3663.

39 T. I. Hasegawa and E. Herbst, *Mon. Not. R. Astron. Soc.*, 1993, **263**, 589.

40 R. T. Garrod and E. Herbst, *Astron. & Astrophys.*, 2006, **457**, 927–936.

41 R. T. Garrod and T. Pauly, *Astrophys. J.*, 2011, **735**, 15.

42 M. S. B. Munson, *J. Am. Chem. Soc.*, 1965, **87**, 2332–2336.

43 N. G. Adams, D. Smith and J. F. Paulson, *J. Chem. Phys.*, 1980, **72**, 288–297.

44 J. Barassin, A. Barassin and R. Thomas, *Int. J. Mass Spectrom. Ion Proc.*, 1983, **49**, 51–60.

45 N. G. Adams, L. M. Babcock, T. M. Mostefaouoi and M. S. Kerns, *Int. J. Mass Spectrom.*, 2003, **223-224**, 459–471.

46 E. Herbst and C. M. Leung, *Astrophys. J.*, 1986, **310**, 378.

47 A. Coutens, J. K. Jørgensen, M. H. D. van der Wiel, H. S. P. Müller, J. M. Lykke, P. Bjerkeli, T. L. Bourke, H. Calcutt, M. N. Drozdovskaya, C. Favre, E. C. Fayolle, R. T. Garrod, S. K. Jacobsen, N. F. W. Ligterink, K. I. Öberg, M. V. Persson, E. F. van Dishoeck and S. F. Wampfler, *Astron. & Astrophys.*, 2016, **590**, L6.

48 N. F. W. Ligterink, H. Calcutt, A. Coutens, L. E. Kristensen, T. L. Bourke, M. N. Drozdovskaya, H. S. P. Müller, S. F. Wampfler, M. H. D. van der Wiel, E. F. van Dishoeck and J. K. Jørgensen, *Astron. & Astrophys.*, 2018, **619**, A28.

49 S. Zeng, Q. Zhang, I. Jiménez-Serra, B. Tercero, X. Lu, J. Martín-Pintado, P. de Vicente, V. M. Rivilla and S. Li, *Mon. Not. R. Astron. Soc.*, 2020, **497**, 4896–4909.

50 V. Wakelam and E. Herbst, *Astrophys. J.*, 2008, **680**, 371–383.